Geophysical Journal International

Geophys. J. Int. (2020) **220,** 2056–2067
Advance Access publication 2019 December 13
GJI Seismology

doi: 10.1093/gji/ggz565

Azimuthal anisotropy in the wider Vienna basin region: a proxy for the present-day stress field and deformation

Sven Schippkus [1], Dimitri Zigone [2], Götz Bokelmann[1] and AlpArray Working Group[3]

[1] *Department of Meteorology and Geophysics, University of Vienna,* 1010 *Vienna, Austria. E-mail: sven.schippkus@univie.ac.at*
[2] *Institut de Physique du Globe de Strasbourg, Université de Strasbourg, EOST, CNRS,* 67081 *Strasbourg, France*
[3] *www.alparray.ethz.ch*

Accepted 2019 December 11. Received 2019 November 7; in original form 2019 August 1

SUMMARY

We infer seismic azimuthal anisotropy from ambient-noise-derived Rayleigh waves in the wider Vienna Basin region. Cross-correlations of the ambient seismic field are computed for 1953 station pairs and periods from 5 to 25 s to measure the directional dependence of interstation Rayleigh-wave group velocities. We perform the analysis for each period on the whole data set, as well as in overlapping 2°-cells to regionalize the measurements, to study expected effects from isotropic structure, and isotropic–anisotropic trade-offs. To extract azimuthal anisotropy that relates to the anisotropic structure of the Earth, we analyse the group velocity residuals after isotropic inversion. The periods discussed in this study (5–20 s) are sensitive to crustal structure, and they allow us to gain insight into two distinct mechanisms that result in fast orientations. At shallow crustal depths, fast orientations in the Eastern Alps are S/N to SSW/NNE, roughly normal to the Alps. This effect is most likely due to the formation of cracks aligned with the present-day stress-field. At greater depths, fast orientations rotate towards NE, almost parallel to the major fault systems that accommodated the lateral extrusion of blocks in the Miocene. This is coherent with the alignment of crystal grains during crustal deformation occurring along the fault systems and the lateral extrusion of the central part of the Eastern Alps.

Key words: Europe; Seismic anisotropy; Seismic interferometry; Seismic noise; Surface waves and free oscillations.

1 INTRODUCTION

Tectonics and seismic activity are consequences of the acting stress field. Gaining insight into the present-day orientation of the stress-field and its evolution over geological time can thus improve our understanding of regional tectonics and future seismicity sharply. Today, the wider Vienna Basin region is one of the seismically most active regions in Austria. It has been subject to major earthquakes in the past, for example the $M \sim 6$ Neulengbach/Ried am Riederberg event in 1590 that caused considerable damage in Vienna (e.g. Gutdeutsch *et al.* 1987; Hammerl & Lenhardt 2013). Due to the limited earthquake record in the area and the sparse knowledge of the regional stress field, there are major uncertainties in seismic hazard assessments in the region. Various techniques such as palaeoseismology have been used to better constrain past and current seismic hazard (Gribovszki *et al.* 2017; Hintersberger *et al.* 2018), however they remain mostly pointwise measurements that lack the coverage over the whole Vienna Basin region. Understanding the stress field better, and which faults may be reactivated to produce significant earthquakes in the near future—as dictated by the stress field—is therefore of great importance for accurate assessment of seismic hazard.

The wider Vienna Basin region lies in the Alpine–Carpathian–Pannonian junction, which is defined by its complex tectonic history. In brief, the N/S-collision of the Eurasian Plate with the African and Adriatic plates resulted in the orogeny of the Alps (e.g. Schmid *et al.* 2004, and references therein). During the Miocene, this led to the lateral northeastwards extrusion of blocks (Gutdeutsch & Aric 1988; Ratschbacher *et al.* 1991; Wölfler *et al.* 2011), accommodated by the major fault systems in the region (see Fig. 1). The sinistral Salzach–Ennstal–Mariazell–Puchberg fault (SEMP in Fig. 1), the Mur–Mürz Line (MML in Fig. 1) and the Vienna Basin Transfer Fault System (VBTFS in Fig. 1) mark the northern edge of extrusion. The dextral Periadriatic Line, and Lavanttal (LA in Fig. 1) fault systems delimit the southern edge of extrusion (Gutdeutsch & Aric 1988). As part of this extrusion, the Vienna Basin (VB in Fig. 1) formed as a thin-skinned pull-apart basin on top of thrust sheets and has undergone a complex history, including formation of the pull-apart structure, fault reactivation, graben formation and normal faulting and rollover (Decker *et al.* 2005; Hölzel *et al.* 2010; Lee & Wagreich 2017).

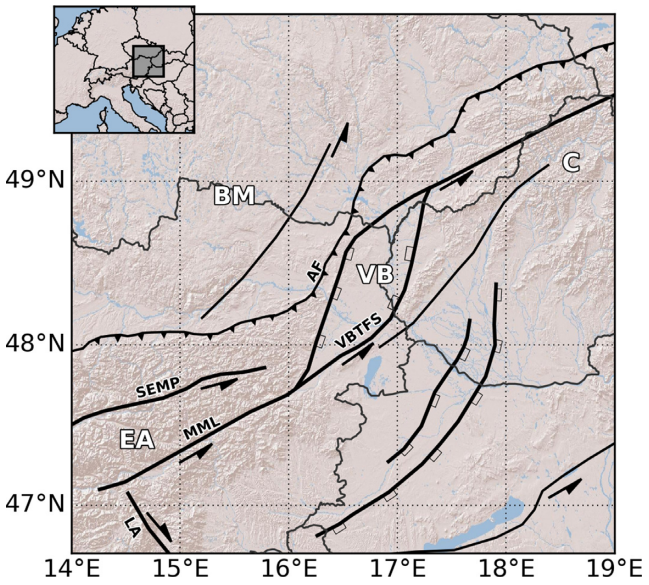

Figure 1. Tectonic sketch map of the study area illustrating the lateral extrusion of blocks (the southeastern half), accommodated by the major fault systems and subsequent formation of the Vienna Basin in the Alpine-Carpathian transition zone. Labelled fault systems: AF (Alpine Thrust-Front), LA (Lavanttal fault), MML (Mur-Mürz-Line), SEMP (Salzach-Ennstal-Mariazell-Puchberg fault), VBTFS (Vienna Basin Transfer Fault System). Labelled major geographical features: Bohemian Massif (BM), Carpathians (C), Eastern Alps (EA), Vienna Basin (VB). Faults are drawn after Peresson & Decker (1997).

The palaeo-stress orientation of maximum horizontal compressive stress σ_H that facilitated the formation of the structures appears to be dominantly oriented N/NNE in the last 17 Ma (see Decker *et al.* 2005 and references therein). These conclusions are consistent with the block model proposed in Gutdeutsch & Aric (1988). Gerner *et al.* (1999), however, modelled the stress field using finite elements based on focal mechanisms, borehole breakouts and *in situ* stress measurements. Their modelling suggests that the present-day σ_H-orientation in our study region is rotated to ∼NW, roughly normal to the Bohemian Massif (BM in Fig. 1). Similarly, Reinecker & Lenhardt (1999) argue that the BM acts as an indenter that results in a ∼NW σ_H-orientation in the eastern part of our study region. This would imply σ_H-orientations almost normal to the MML and nearby fault systems, raising the question why these faults are seismically active today. The focal mechanisms used in these studies (Gerner *et al.* 1999; Reinecker & Lenhardt 1999) are mainly sinistral strike-slip mechanisms along the MML. In contrast, Bada *et al.* (2007) present a smoothed map of an updated collection of stress-field measurements and report ∼N-orientations of σ_H in the west and north of our study area, and ∼NE-orientations in the east and south. Robl & Stüwe (2005) report similar orientations based on viscous thin sheet simulation. These orientations are roughly normal to the Alps (instead of the BM) and are indeed compatible with the observed seismic activity along the MML. More recently, seismicity along the MML and in the region has been found to be a combination of strike-slip-, normal- and thrust-faulting events (Brückl *et al.* 2014), which raises further questions about the present-day orientation of σ_H.

In this study, we investigate the azimuthal anisotropy of Rayleigh waves in the region to gain insight into the orientation of the stress-field and historical deformation. Our work focuses on using an existing high-quality isotropic velocity model for the Vienna Basin region (Schippkus *et al.* 2018) in a new sequential inversion approach which allows to extract and study the anisotropic structure of the crust. For this, we rely on two mechanisms that generate seismic anisotropy, and faster propagation of Rayleigh waves along σ_H: in the upper crust, cracks open in the direction perpendicular to σ_H, if the lowest compressive stress σ_3 is horizontal. Seismic waves travel faster along that axis, because fluid-filled cracks reduce seismic velocities in the direction normal to it (Nur 1971). On the other hand, deformation can align crystals, especially in the lower crust (Barruol & Kern 1996), which may cause seismic anisotropy. Because the Rayleigh waves we utilize are retrieved from ambient-noise cross-correlations, which means they represent estimated Green's functions between receiver pairs (Nakata *et al.* 2019, and references therein), effects on the propagation speed are contained within the study area and they are sensitive to anisotropy in the area.

In the following, we describe our approach, the directional dependence of Rayleigh wave velocities, how they may relate to azimuthal anisotropy, and finally discuss limitations and advantages of our approach as well as our observations of the present-day stress field and historical deformation.

2 DATA AND METHOD

The data used in this study are the fundamental-mode Rayleigh-wave group velocities presented in Schippkus *et al.* (2018). Here, we analyse the measured group velocities u_m, predicted group velocities from the isotropic model u_p, and their residuals $u_r = u_p - u_m$. In Schippkus *et al.* (2018), interstation group velocities are estimated from ambient-noise cross-correlation functions (CCFs) for 1953 station pairs. 187 850 (59.6 per cent) interstation measurements pass the quality- and statistics-based selection procedure, with the number of remaining measurements depending on period (Fig. 2). These measurements were previously used to compute an isotropic shear-velocity model of the region (Schippkus *et al.* 2018). The interstation paths remaining after selection show no significant bias in available azimuth for the periods discussed later in this study (5–20 s, Fig. 2). At longer periods ($T > 20$ s), the criterion that limits minimum interstation distance results in a skewed distribution in azimuth, with only certain azimuths being available for long interstation distances (Fig. 2f). We therefore refrain from interpreting those periods in greater detail.

We parametrize azimuthal anisotropy of Rayleigh wave group velocities following Smith & Dahlen (1973) by

$$u\ (\Theta) = u_0\ + A * \cos(2 * (\Theta - \varphi_2)) + B * \cos(4 * (\Theta - \varphi_4)),$$

with the isotropic velocity u_0, the amplitude A and phase shift φ_2 of the 2Θ-term and the amplitude B and phase shift φ_4 of the 4Θ-term. To stabilize the fitting, we use the medians of azimuth-binned group-velocities (5°-bins) and weigh them by their respective standard-deviations (see Fig. S1). While we account for the 4Θ-term during the curve-fit (Fig. S2), in this study we aim to only interpret the 2Θ-term.

To learn about the spatial distribution of A and fast orientation φ_2 in the study area, we regionalize the approach, that is we estimate the azimuthal anisotropy in smaller subareas. For this, an evenly spaced grid (in latitude and longitude) of overlapping cells is defined across the region. For each of those cells, we estimate the directional dependence, as described above, of those interstation paths that cross the cell. The median for each azimuth-bin is measured from interstation group velocities weighted by their path-length inside the

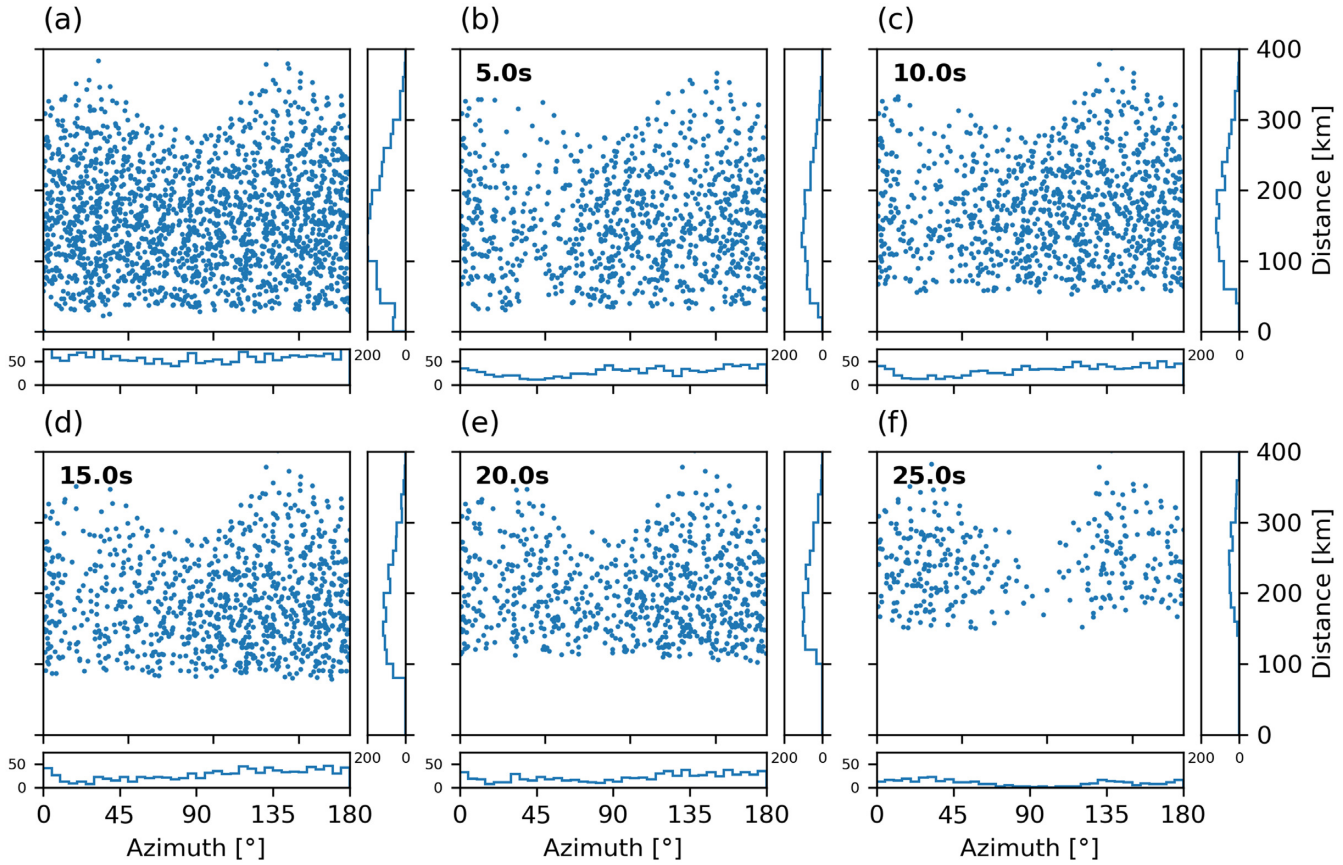

Figure 2. Interstation geometry for all available station pairs (a) and the station pairs remaining after selection criteria applied during group velocity measurements for different periods (b–f). At shorter periods, slight bias of removal for interstation orientations ∼NE due to decreased signal-to-noise-ratio of CCFs that are oriented normal to the main noise source direction. Increasing minimum interstation distance with increasing period to due to the minimum-wavelength criterion, leading to strong azimuth-bias at 25 s. For more details on the retrieval of group velocities, see Schippkus *et al.* (2018).

cell. More precisely, for each of those cells, all 5 km cells (from the parametrization of the isotropic inversion of Schippkus *et al.* 2018) contained within the large cell are checked for crossing paths and these paths' group velocities and azimuths are taken as data points. Therefore, paths that cross n 5 km cells within a large cell result in n velocity-azimuth data points for that cell, that is the velocity medians are weighted approximately by their path-length within the larger cell.

3 RESULTS

In the following, we present our findings on the directional dependence of measured group velocities (4.1), of modelled group velocities from the isotropic velocity model (4.2), and of group velocity residuals (4.3).

3.1 Measured group velocities

The directional dependence of group velocities, measured on all paths for a given period (Fig. 3a), shows that fast orientations vary from –5° to 50° (S–N to SSW–NNE), depending on period. In the following, we will refer to them only by one direction, in this case N–NNE. The amplitude of the directional variation is larger for shorter periods (∼6 per cent at 5 s), decreasing with period and reaching a plateau at around 10 s, where lower amplitudes of 1–2 per cent are observed. At periods larger than 20 s, the amplitude increases again up to ∼4 per cent. All shown error bars indicate one standard deviation. There is an interdependence of errors in direction and amplitude with the amplitude A itself. The lower the amplitude A, the less-well-determined A and φ_2 are. This leads to very high errors (±3 per cent) for amplitudes <2 per cent, meaning that no directional dependence ($A = 0$) of group velocities is consistent with the observations at least for some periods (10–20 s, Fig. 3a).

We regionalize the directional dependence, as described above, of the measured group velocities for 5 s (Fig. 4a) and 20 s (Fig. 4e) to represent the shallow (5 s) and mid-crustal structure (20 s). We find that these periods show distinctly different behaviour in our approach that is representative for the entire period-range. Here, we choose to parametrize the grid-cells with 2° width and height, and 85 per cent overlap. This dense distribution of cells is used to more clearly illustrate the observations we make and support the arguments we bring forward. For the purpose of discussion, however, we will later apply a coarser grid to prevent overinterpretation given the limitations in lateral resolution of our approach. The most striking feature of the regionalized fast orientations is that they seem to form a tangential shape around the southeastern part at 5 s (Fig. 4a). The 'centre' of this shape is roughly collocated with the major sedimentary basins in the region [VB and Little Hungarian Plain (LHP)], marked by the two low-velocity features in the isotropic model of Schippkus *et al.* (2018) (Fig. 4d). For a given 2°-cell, the paths across sedimentary basins are generally slower

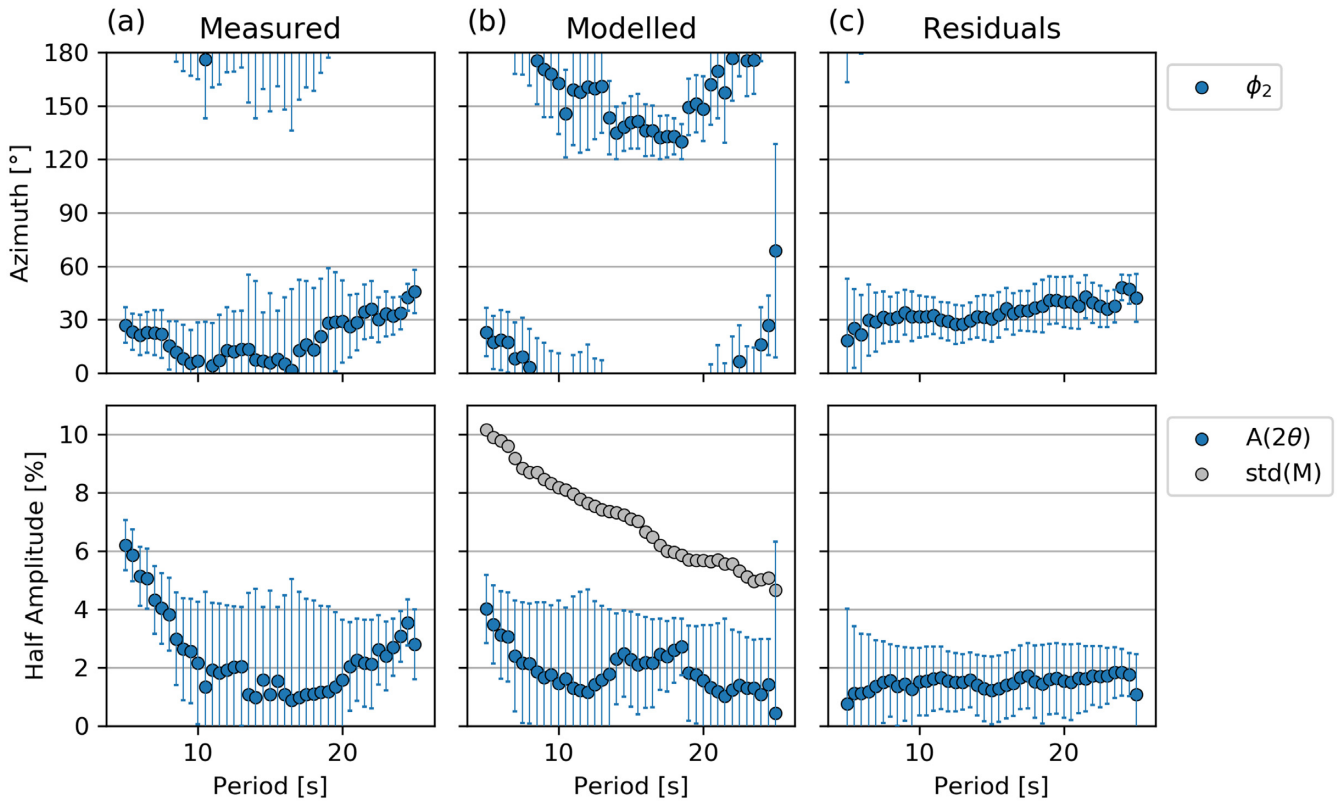

Figure 3. Directional dependence (2θ-terms) of group velocities for measured (a), modelled (b), and residual (c) group velocities. (a) Measured group velocities show N–NNE fast orientations (φ_2) for all periods. Amplitude decreases with period until plateau is reached. (b) Group velocities modelled from the isotropic velocity model also show directional dependence. Similar trend in amplitude as (a). Decreasing amplitude of velocity model (represented by standard deviation $\boldsymbol{std}(\boldsymbol{M})$, grey points) with period may explain decreasing amplitude of the 2θ-term. (c) Residual group velocities show stable NNE fast orientation that rotates slightly towards E with increasing period. Lower, but stable amplitudes for all periods around 1–2 per cent.

than paths across crystalline basement rocks of the BM. This results in a pattern where fast orientations are oriented tangentially around the low-velocity anomalies. The same effect is visible for 20 s (Fig. 4e) for which only the VB and underlying structure remains as a dominant low-velocity anomaly (Fig. 4h), resulting in a smaller radius of the tangential feature (Fig. 4e). These observations suggest that the regionalized fast orientations determined from measured interstation group-velocities may be dominated by isotropic effects—the heterogeneous distribution of velocities—rather than anisotropic structure.

3.2 Modelled group velocities

To test this hypothesis, we determine the directional dependence of group velocities as predicted by the isotopic velocity model (Schippkus *et al.* 2018), first on the entire region. We find that the isotropic model also predicts a directional dependence of Rayleigh wave velocities (Fig. 3b), although different from the measured group velocities (Fig. 3a). Fast orientations are varying over a larger range (–50° to 65°) and amplitudes are generally lower, especially at short (5–10 s) and long periods (20–25 s). At intermediate periods (10–20 s), a slight increase in amplitude is observed, corresponding to a change in fast orientation to NW. However, an amplitude decrease with period for short periods (5–10 s) is present for both the measured (Fig. 3a) and predicted group velocities (Fig. 3b). The standard deviation of the isotropic velocity model $std(M)$ (Fig. 3b) suggests that the decrease of amplitude with period may be partly explained by the decreasing model amplitude. The amplitude of directional dependence may be influenced by the velocity-contrasts within the model, pointing again to isotropic effects rather than anisotropic structure.

The regionalized fast orientations as estimated from modelled group velocities (Figs 4b and f) show striking similarity with those estimated from measured group velocities (Figs 4a and e), especially for 5 s (Figs 4a and b). At 20 s (Figs 4f and e), some differences are visible, but the overall pattern is very similar, with the main feature—fast orientations tangential to the low-velocity anomalies—well visible. Our hypothesis that the distinct pattern of fast orientations is largely explained by the heterogeneity of isotropic velocities seems to hold, given how closely the patterns from measured and modelled group velocities resemble each other.

3.3 Group velocity residuals

As shown above, the fast orientations estimated from measured group velocities appear to be dominated by isotropic effects. Therefore, we analyse the residuals after isotropic inversion, that is the difference of modelled and measured group velocities, to extract azimuthal anisotropy. These residuals contain only effects that the isotropic model cannot explain, that is errors in data (e.g. inaccurate measurements), errors in the model (e.g. invalid assumptions, smoothing) and effects of the anisotropic structure, the target of our study. The group velocity residuals (Fig. 3c) show a stable NNE (∼30°) fast orientation φ_2 that rotates slightly towards east (from 25° to 50°) with increasing period. The amplitude A is relatively stable around 1.5 per cent and no longer exhibits a decreasing trend.

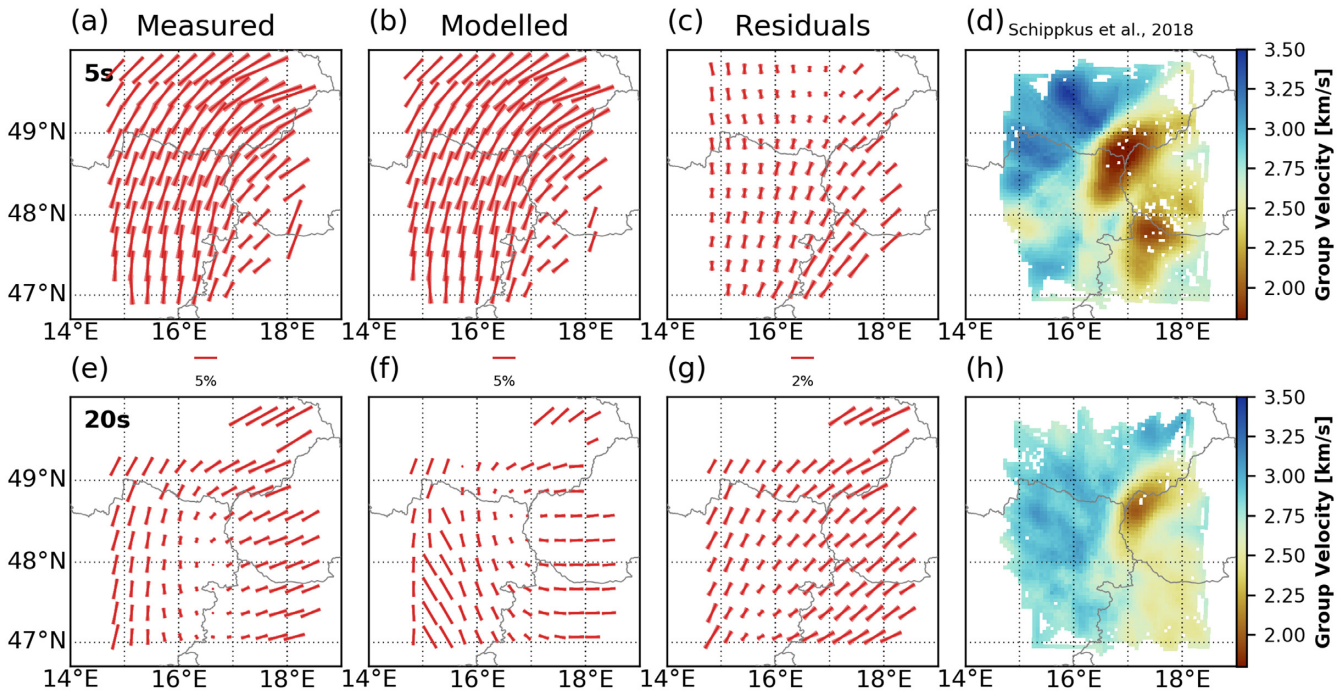

Figure 4. Regionalization of fast orientations for measured (a, e), modelled (b, f) and residual group velocities (c, g) in a grid of 2°-cells, overlapping with 85 per cent at 5 s (top row) and 20 s (bottom row). The group velocity maps (d, h) of Schippkus *et al.* (2018) allow to interpret the observed features. Fast orientations (φ_2) estimated from measured and modelled group velocities show a very similar pattern. Striking is the tangential alignment of fast orientations around the major low-velocity anomalies, explained by isotropic effects (fast paths within a cell are those that do not cross the low-velocity anomalies). Locally, amplitudes can be considerable ($A \sim 10$ *per cent*). Residual group velocities at 5 s (c) show a smoothly varying distribution of fast orientations, although fast orientations in the Southeast that are similar to both (a) and (b) remain. At 20 s (g), fast orientations from residuals are universally aligned ∼NE.

The regionalized fast orientations of residual group velocities at 5 s (Fig. 4c) show a distribution that still appears to contain some previously observed features, but it is overall very different from the patterns observed for measured (Fig. 4a) and modelled (Fig. 4b) velocities. Most notably, the NE φ_2-orientation at the southeastern edge, present for both measured and modelled group velocities (Figs 4a and b), remains consistent, although with reduced amplitude. The clear tangential pattern observed previously (Figs 4a and b) is no longer present and instead a spatially-coherent rotation of the fast orientation (N–NE) from west to east is visible. At 20 s (Fig. 4g), the fast orientations are spatially coherent NE over the entire region with only minimal variation. Still, a very slight tangential trend appears to be present around the low-velocity anomaly in the NE, but the effect is negligible compared to previous observations (Figs 4a, b, e and f).

3.4 Impact of smoothing constraint

As mentioned above, the smoothing constraint during the isotropic inversion may propagate isotropic effects into the residuals. Because we have direct control over this parameter, we can test how it may bias our measurements. For this, we invert the measured group velocities with weaker smoothing and compare to our results with stronger smoothing (Fig. 5). Each panel (a–d) shows the regionalized fast orientation measured from group-velocity residuals on the left-hand side. On the right-hand side, we show the inverted group-velocity residuals, where the residuals are used as input in a second isotropic inversion to regionalize them. The second inversion is parametrized the same as the first inversion. This allows insight into whether the residuals are randomly distributed or heavily influenced by the isotropic velocity structure.

With stronger smoothing, as used in this study and Schippkus *et al.* (2018) (smoothing factor $a = 35$), the model does not fully explain the measured group velocities. The model velocities in the VB and LHP are not low enough to fully account for the measured velocities (a, b in Fig. 5a). Similarly, the model velocities in between the basins are too low to explain the data (c in Fig. 5a). Here, the Little Carpathians separate the two basins. This mountain range is geographically too narrow to be properly represented with the chosen smoothing constraint. This suggests that isotropic effects do indeed propagate into the residuals. Isotropic inversion with a weaker smoothing constraint ($a = 10$, Fig. 5b) results in a more random distribution of residuals. They still contain isotropic effects, but the effects are no longer as dominant in the model. The retrieved azimuthal anisotropy from those residuals is generally much weaker and constrained more poorly (Fig. 5b) and may locally even change orientation dramatically. Note that the amplitude of the directional dependence decreases with weaker smoothing, because a weaker smoothing constraint results in a better data-fit and therefore lower residuals. The fast orientations (Fig. 5b), however, still appear to be mostly consistent with the findings for stronger smoothing (Fig. 5a).

At 20 s, similar observations can be made. The model velocities near the VB are also too low to fully explain the data (Fig. 5c) and with weaker smoothing the residual distribution appears more random (Fig. 5d). However, the isotropic effects are not as impactful on the regionalized fast orientations at 20 s as compared to 5 s. This is evident by the minimal effect of the smoothing constraint on the retrieved fast orientations (Figs 5c and d). Importantly, the tangential-trend-argument introduced above does not explain the

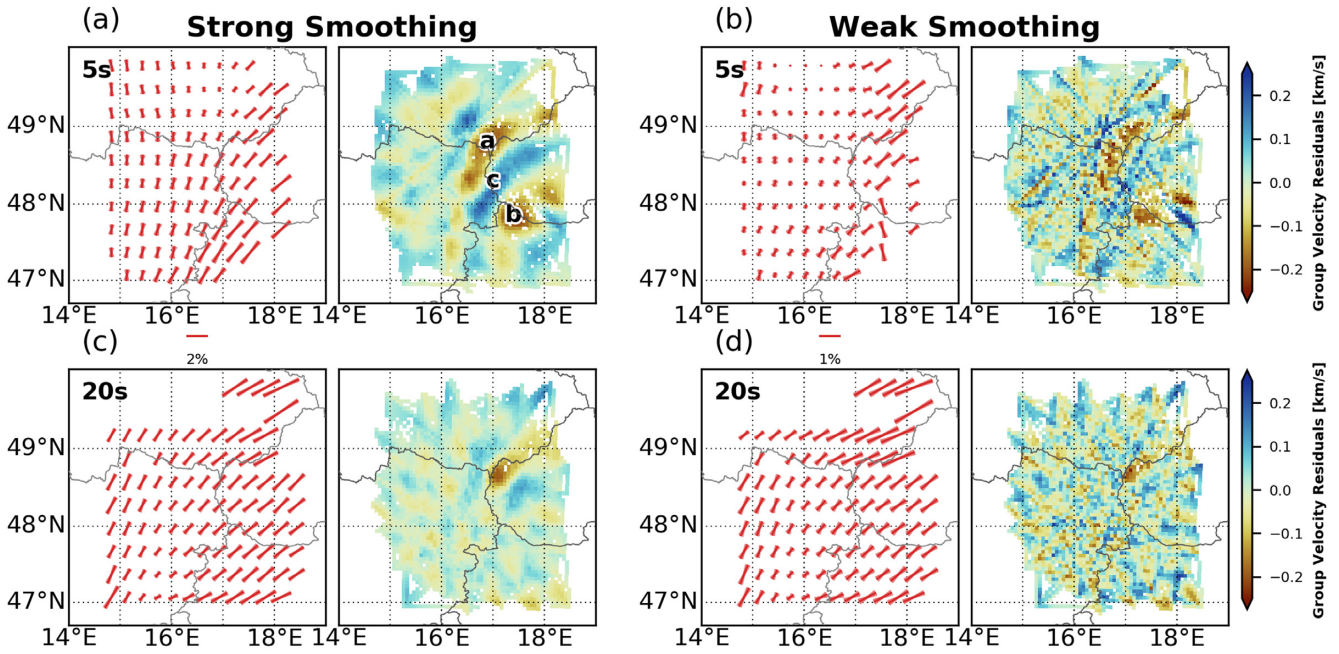

Figure 5. Impact of the smoothing constraint applied during isotropic inversion on retrieved azimuthal anisotropy from group-velocity residuals. Each panel (a–d) shows the regionalization of anisotropy (left-hand side) and the inverted group velocity residuals, in a second isotropic inversion. Left-hand panel: results for the stronger smoothing constraint used in Schippkus *et al.* (2018) ($a = 35$). Right-hand panel: results for a weaker smoothing constraint ($a = 10$). With stronger smoothing, isotropic velocity structure carries over into the residuals (a, c) and may continue to bias estimation of anisotropy. Distribution of residuals with weaker smoothing (b, d) appears more random and less representative of isotropic structure, although some influence remains. At 5 s, the smoothing constraint has strong impact on retrieved anisotropy. At 20 s, the smoothing has only minimal impact on the retrieved directions. Note the different scale for strong and weak smoothing, and that the amplitude of anisotropy decreases with weaker smoothing.

consistently observed NE fast orientations across the entire region (Figs 5c and d).

4 DISCUSSION

We split the discussion into two parts: a methodological and a structural part. In the methodological part, we aim to discuss the assumptions, robustness, and limitations of our approach in order to argue that we do indeed observe anisotropic structure in residual group velocities. In the structural part, we discuss our findings in the geological and tectonic context.

4.1 Methodology

The group velocity $u(\vec{x},\ \Theta)$ at a location $\vec{x}$ is the sum of two contributions

$$u\left(\vec{x},\ \Theta\right) = u_{iso}\left(\vec{x}\right) + u_{aniso}\left(\vec{x},\ \Theta\right),$$

with the isotropic part $u_{iso}(\vec{x})$ and the anisotropic part $u_{aniso}(\vec{x},\ \Theta)$, which is dependent on the direction of wave propagation Θ. The approach presented in this paper is a sequential one based on the assumption that a thoroughly conducted isotropic inversion (as done in Schippkus *et al.* 2018) retrieves the isotropic structure $u_{iso}(\vec{x})$, whereas the residual group velocities of the isotropic inversion are primarily sensitive to the anisotropic velocity structure $u_{aniso}(\vec{x},\ \Theta)$.

The observed anisotropy on the order of a few per cent raises the question about the accuracy of our traveltime measurements and potential biases therein. Errors on this order are negligible for interpreting tomographic images of the crust (Schippkus *et al.* 2018), but this is still to be seen in the context of anisotropy.

A non-uniform distribution of noise sources might, in extreme cases, introduce traveltime errors on the order of a few per cent in Green's functions estimated from cross-correlations of the ambient seismic field (Tsai 2009; Froment *et al.* 2010). Froment *et al.* (2010) find faster velocities for station pairs that are aligned roughly normal to the dominant noise source direction. However, if the wavefield is sufficiently scattered, that is if not ballistic waves are cross-correlated but their coda, this error is reduced to almost zero (Froment *et al.* 2010). The primary (∼14 s) and secondary (∼7 s) microseism peaks are generated by different mechanisms (Longuet-Higgings 1950; Hasselmann 1963) and originate at different locations (Juretzek & Hadziioannou 2016), resulting in a less-well-defined dominant noise source direction. Furthermore, we use data recorded over 2 yr to retrieve estimated Green's functions, accounting for different dominant noise source regimes, which are different in winter and summer months. Therefore, in our case, the wavefield likely consists of a variety of ballistic and scattered waves arriving from different directions. We believe that this alleviates potential traveltime errors.

This study is based on group velocities measured on estimated Green's functions that contain Rayleigh waves. Group-velocity measurements are not very precise, because the peak of the envelope of a filtered waveform is picked as an estimate for group-velocity (Dziewonski *et al.* 1969). The distribution of residuals in Fig. S1 indicates that measurement errors give rise to velocity errors that are not larger than 0.2 km s^{-1}, and probably smaller than that (since unmodelled effects are also included). One might think that longer periods would be associated with less precise measurements, due to the filtre-width increase with wavelength. Fig. S1 suggests though that this does not seem to be the case. Overall, the uncertainties are not large.

Some of the errors that enter prior to the retrieval of residual group velocities are on the order of the measured effect of a few per cent. To test for the significance of our results, we model the worst-case scenario: What if the combination of all errors results in entirely random group-velocity residuals that are no longer representative of any physical feature? For this, we compute 10 000 sets of randomly distributed interstation residuals for each period, using the available interstation geometry per period and measure azimuthal anisotropy on them (Fig. S3). We find that our results, although small in amplitude and subject to potentially significant errors, are extremely unlikely to be a result of chance, especially given the consistency of our results over the period range. This gives more credibility to our results and agrees with our previous considerations that the errors we introduce are likely smaller than the amplitude of anisotropy A. This approach does not account for the propagation of physical effects other than from anisotropic structure into the residuals, though. Our tests on the impact of the smoothing constraint (Fig. 5) should give confidence that the isotropic velocity structure does not heavily influence the retrieved fast orientations, at least for periods longer than 5 s.

The interpretation of group velocity residuals in terms of azimuthal anisotropy relies not only on negligible propagation of isotropic effects into the residuals, but also on a purely isotropic model that does not already account for anisotropic effects. As discussed in Schippkus *et al.* (2018), we believe this model is a good representation of the isotropic velocity structure of the wider Vienna Basin region. In addition to the arguments presented in Schippkus *et al.* (2018), which include surface geology, velocity contrasts at known faults, and gravitational anomalies to confirm the lateral extent of the observed features, as well as ground truth from boreholes and refraction profiles to confirm the depth-extent, the refraction profile 7R (Dvorak *et al.* 1990) is also in good agreement with the imaged deep low-velocity anomaly in the Vienna Basin. Therefore, we believe that there is no significant influence of anisotropy on the isotropic velocity model.

In recent literature, it is common practice to interpret azimuthal anisotropy directly from measured group velocities (e.g. Mordret *et al.* 2013; Zigone *et al.* 2015; Taylor *et al.* 2019). In this study, we show that interpretation of measured group velocities in terms of anisotropic structure can be misleading, as the heterogeneities of the isotropic velocity structure can dominate the apparent fast orientations. This can occur even with a relatively homogeneous distribution of path geometries (Fig. 2). We suggest that a simple 2-step approach of isotropic inversion and interpretation of residuals will result in more confident estimates of anisotropic structure. An alternative approach would be to perform a simultaneous inversion, as has been done for the Swiss region by Fry *et al.* (2010). They have tested the trade-off between isotropic and anisotropic terms, and found that there are indeed such trade-offs for experimental conditions that are somewhat similar to ours (e.g. noise-based measurements, study region size, number of stations). This confirms us in our sequential approach to analyse anisotropic effects that cannot be explained by the isotropic model.

4.2 Geological and tectonic context

These arguments lead us to conclude that the group velocity residuals contain mainly anisotropic effects (and not errors or biases), and they can thus be interpreted in terms of structure and tectonics.

In the study area, most of the major fault systems (SEMP, MML, VBTFS, LA, see Fig. 1) accommodate the lateral extrusion of blocks during the Miocene (Gutdeutsch & Aric 1988; Ratschbacher *et al.* 1991), a consequence of the Africa–Eurasia collision and the Alpine orogeny (e.g. Schmid *et al.* 2004, and references therein). These faults and with them the extruded blocks are oriented towards NE, roughly matching the fast orientations we observe on the group velocity residuals across all available periods (Figs 3c, 4 and 6). We note an overall rotation to more eastern orientations at longer periods.

The most likely explanation for the consistent change in fast orientation towards NE with increasing period (Figs 3c, 4 and 6) is the depth sensitivity of Rayleigh waves (Fig. 7a). The two periods we will discuss here (5 and 20 s, Fig. 6) have their maximum sensitivity at depths of ∼2 and ∼15 km, respectively (Fig. 7a). The full range of studied periods are presented in Fig. S4. Seismic anisotropy in the crust generally consists of two parts, a) stress-related and b) texture-related anisotropy (Fig. 7b; Kern 1990). The effect of crack-induced (i.e. stress-related) anisotropy is confined to the topmost kilometers in the crust (see also Nur & Simmons 1969), while texture-related anisotropy can occur at any depth. Whether anisotropy appears in seismological observations depends largely on processes that align the microscopic anisotropy at spatial scales comparable to seismic wavelengths (kilometers to tens of kilometres).

There are two candidates for such aligning processes, (a) cracks in the topmost kilometers may be aligned by the tectonic stress field and (b) shear in the lower crust may align minerals spatially. Crack-related anisotropy is therefore likely to appear in measurements for shorter periods (especially around 5 s) making it possible to characterize the present-day stress-field acting within the topmost kilometers. This has been confirmed by borehole studies (e.g. Zinke & Zoback 2000). If the measurements do not pertain to the vicinity of major faults, seismic fast orientations directly give the orientation of maximum horizontal compressive stress σ_H (Boness & Zoback 2006). Longer periods (more than ∼10 s), on the other hand, are no longer sensitive to cracks, as potential cracks are likely closed due to higher lithostatic pressure at depths larger than a few kilometres (Fig. 7b). The longer periods are most likely sensitive to the alignment of crystals in the deeper crust during long periods of deformation (Barruol & Kern 1996), i.e. the deformation associated with the deeper extent of the faults and the lateral extrusion of blocks. Rayleigh waves can in principle distinguish crack-induced anisotropy from that created by deeper crustal deformation. This allows insight into each of the two processes separately.

In the very shallow crust (Fig. 6a), two regions of common fast orientation φ_2 can be distinguished. In the west, and especially to the West of the Vienna Basin (VB), fast orientations align along ∼N. To the east, roughly south of the AF (Fig. 6a) fast orientations are rotated towards NE. Some of these φ_2-orientations agree with the stress-field orientations of Reinecker & Lenhardt (1999), especially in the southwestern region around the SEMP and the western part of the MML (Fig. 8). They are also consistent in tendency in the Bohemian Massif, with an observed rotation to NNW. The agreement is lower for the Vienna Basin area, the eastern MML, and VBTFS, where Reinecker & Lenhardt (1999) also show NNW orientations. There, the stress-field orientations they report are however almost normal to the MML and VBTFS (Fig. 8), inconsistent with its seismic activity. Their orientations would correspond to angles of the stress field with the MML of around $\alpha \sim 20^\circ$, which would require that the fault moves despite rather low values of the coefficient of internal friction (Fig. 9). Such orientations are unlikely to explain the seismic activity along the MML. The results in Reinecker & Lenhardt (1999) are based on 28 individual focal mechanisms and 9 borehole breakout measurements, which scattered strongly around

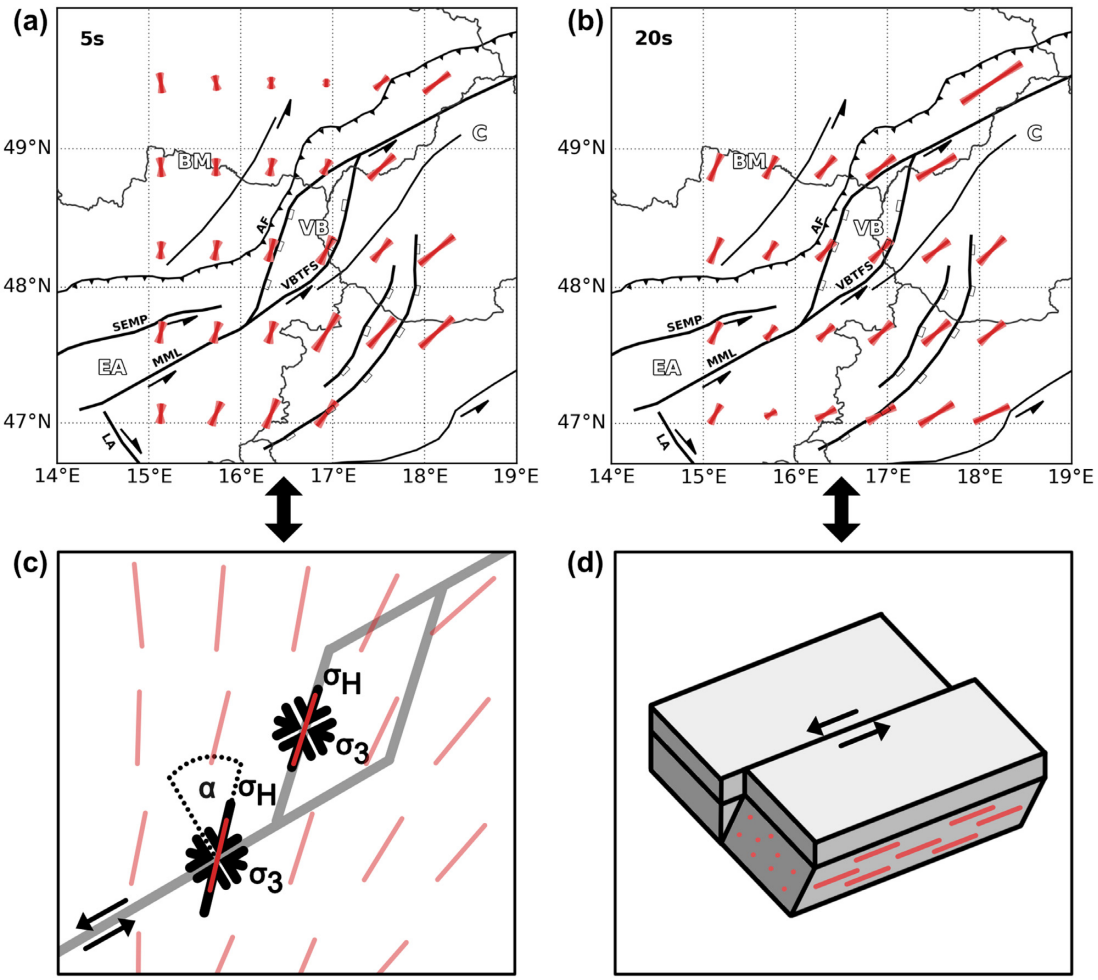

Figure 6. Regionalized azimuthal anisotropy of Rayleigh waves (a, b) and their shallow (c) and mid-crustal (d) interpretations. (a) At 5 s—sensitive to the top few kilometers of the crust—fast orientations align with the orientation of the maximum horizontal compressive stress $\boldsymbol{\sigma_H}$, due to formation of cracks. (b) At 20 s—sensitive to mid-crustal depths—there is a rotation of fast orientation towards northeast, almost parallel to the faults that accommodate lateral extrusion of blocks. (c) Near the MML, fast orientations $\boldsymbol{\varphi_2}$ are oriented within 30–45 degrees to the fault, which is compatible (for $\boldsymbol{\sigma_H}$) with reactivation of slightly-weakened rocks (see Fig. 9). Near the normal faults of the VBTFS $\boldsymbol{\varphi_2}$ are oriented essentially parallel to them. The horizontal principal stress are indicated for both the strike-slip ($\boldsymbol{\sigma_H = \sigma_1}$) and the normal faults ($\boldsymbol{\sigma_H = \sigma_2}$). (d) Mid-crustal deformation due to lateral extrusion results in alignment of crystals in the direction of relative motion, leading to fast orientations along the axis.

the (known) orientation of the fault. These few measurements likely do not sample the whole system.

Bada *et al.* (1998) and Gerner *et al.* (1999) have investigated the stress field in a larger area including the VB region, but their observations also do not seem to obey these constraints of seismic activity. There is a large mismatch between their modeled and the observed stress-field orientations in that region. Stress data from the oil industry scatter a lot (and possibly vary spatially), but they often show ∼N–S orientations of σ_H (e.g. Marsch *et al.* 1990; Decker *et al.* 2005; Decker & Burmester 2008; Schippkus *et al.* in press).

The stress-field orientations reported in Robl & Stüwe (2005) and Bada *et al.* (2007), however, are largely consistent with our results (Robl & Stüwe (2005) shown in Fig. 8). These studies report similar orientations in the region of interest based on two independent approaches: the results of Bada *et al.* (2007) are based on a smoothed map of point-wise measurements of the stress-field orientation over a larger region. In the wider Vienna Basin region, however, these measurements scatter considerably and are sparse (e.g. Bada *et al.* 2007; Heidbach *et al.* 2018). Robl & Stüwe (2005) performed a viscous thin sheet simulation, constrained by geological and tectonic considerations, and consistent with the velocity field measured by GPS stations. There is some disagreement between the two studies in the northeast, they are almost perpendicular to each other. At the northeastern edge of our study area, our results show orientations very similar to Robl & Stüwe (2005) (Fig. 8), but are based only on few data (as can be seen by unresolved pixels in the shear-velocity model in Fig. 4d). In the northwest, our orientations deviate slightly from the results of Robl & Stüwe (2005) (∼NNW versus ∼NNE orientations), but their ∼NNW-orientations lie within one standard deviation of our orientations (marked by light red colour in Fig. 8).

Our results show seismic fast orientations to have angles with the MML α between 30° and 45° (Figs 6a and c). These are reasonable values for an 'actively moving' fault (see Fig. 9), which is characterized by the occurrence of earthquakes (or fault creep). Near the normal-fault sides of the VBTFS, the fast orientations are essentially parallel to the faults, which is not surprising, if the fast orientation φ_2 indeed represents σ_H (as shown by Zinke & Zoback 2000). These observations are illustrated in Fig. 6(c), where we present a schematic view of how the fast orientations φ_2 (and thus

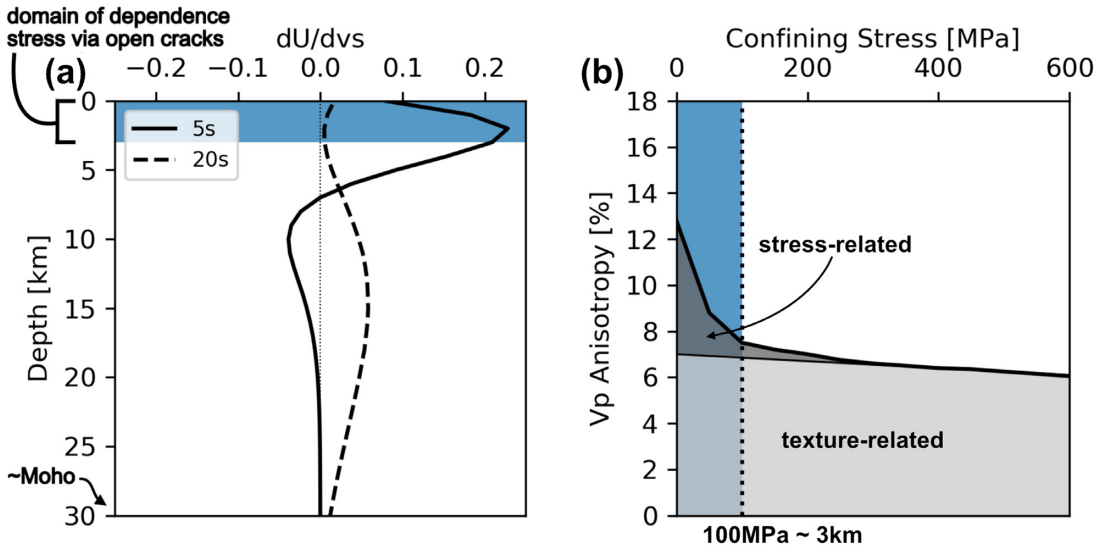

Figure 7. Sensitivity of Rayleigh waves to anisotropic effects. (a) Group-velocity sensitivity to shear-velocity structure for the mean velocity model of the region (Schippkus *et al.* 2018). The period range in this study probes the crustal structure, with maxima at different depths. At 5 s Rayleigh waves are most sensitive to shallow crustal structure (top ∼5 km), whereas at 20 s they are more sensitive to the deeper crustal structure (below ∼10 km). (b) General dependence of seismic anisotropy on confining pressure (redrawn after Kern 1990). The trend is analogous for shear velocities (e.g. Kern & Wenk 1990). There are two types of seismic anisotropy, stress-related versus texture-related. Stress-related anisotropy is due to the existence of open cracks, and it is thus confined to the topmost kilometers (100 MPa confining stress corresponds roughly to 3 km depth).

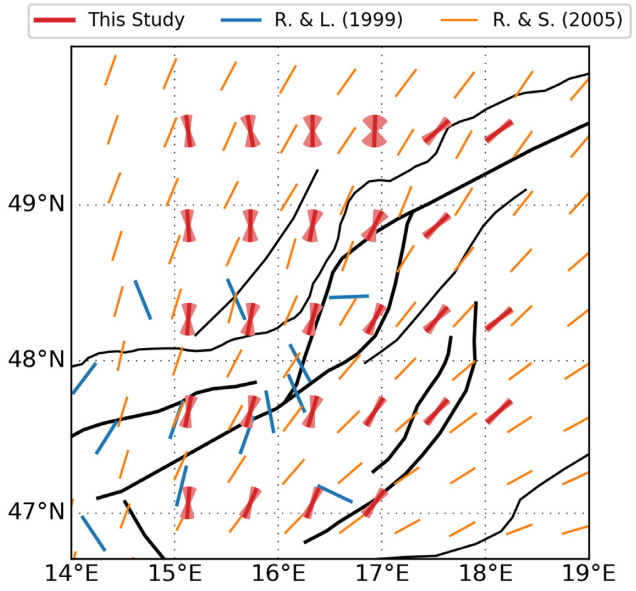

Figure 8. Orientation of the maximum horizontal compressive stress σ_H from this study, Reinecker & Lenhardt (R. & L. 1999) and Robl & Stüwe (R. & S. 2005). Our results show limited agreement with Reinecker & Lenhardt (1999), whereas they are highly consistent the orientations reported by Robl & Stüwe (2005).

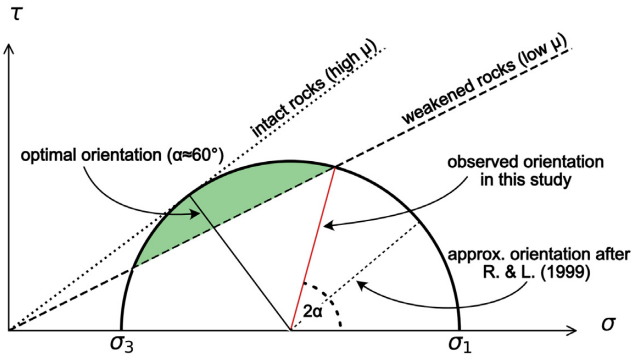

Figure 9. Schematic Mohr's circle to illustrate the interaction between stress-field and seismic activity at the MML fault. The repeatedly ruptured and therefore weakened rocks of the MML likely have reduced coefficients of internal friction μ. This allows a wider range of rupture plane orientations to be active (green area), beyond optimally oriented faults. Therefore, the fast orientations (and hence stress field) we observe in this study is compatible with the recent seismic activity along the MML, one of Austria's seismically most active faults.

orientation of σ_H) likely relate to the geometry and different faulting regimes of the MML and VBTFS.

These considerations suggest that the φ_2-orientations we find do indeed indicate the orientations of σ_H, and with that a more coherent orientation of σ_H ∼NNE–SSW across the region (Figs 6a and c) similar to Robl & Stüwe (2005), as compared to the strong lateral change of σ_H reported by Reinecker & Lenhardt (1999). This is of much interest especially for an area like the wider Vienna Basin region, where many aspects of the stress field are not well-known.

Our reported σ_H-orientations are consistent with the geometry of the different fault systems (see Fig. 6c), even though the type of stress-field regime (strike-slip-, normal- or reverse-faulting) appears to vary at close spatial distance, indicated by the complexity of faulting in the area. A simple schematic model like the one in Fig. 6c cannot—and is not intended to—fully capture the spatial complexity nor the necessary time-dependent deformation. Some of this complexity (or time-dependence) may however be reflected by indications of a vertical rotation of σ_H in the crystalline basement compared to the overlying rocks across individual faults such as the Steinberg fault (Marsch *et al.* 1990; Decker *et al.* 2005).

From Fig. 6(a) we further note that amplitudes of azimuthal anisotropy are smaller in the BM and higher to the east, in the sedimentary basins (VB, LHP). However, at this point it seems beyond

our goals to speculate about whether that difference in amplitude could be explained by the difference in susceptibility of crystalline and sedimentary rocks to crack-formation, or the increased stresses in the east due to the stronger tectonic deformation in that region (e.g. ongoing influence of lateral extrusion).

To understand the general characteristics of the stress field, it appears useful to look at the larger regional scale. Reinecker *et al.* (2010) and Heidbach *et al.* (2018) show highly consistent orientations of σ_H ∼N–S in the Molasse region that rotate towards west into NNW-orientations—suggesting an important role of the gravitational potential of the Alps. Towards the east, σ_H rotates into NNE-orientations, as reported in Reinecker & Lenhardt (1999) at least for Upper Austria. Our results suggest that the stress field continues its consistent trend even further to the east towards the eastern edge of the Alps and into the Alpine-Carpathian transition zone, which supports the strong impact of gravitational forces to the regional stress field. This has been proposed before by Bada *et al.* (2007).

In the deeper crust (Fig. 6b), we find fast orientations generally towards NE. These orientations inside and at the edge of the extruded blocks are almost parallel to the major sinistral strike-slip fault systems (SEMP, MML, VBTFS in Figs 1 and 6). To the north of these fault systems, ∼NNE fast orientation seem to be dominant. At the larger depths to which Rayleigh waves are sensitive at these periods, this anisotropy could very-well be caused by crystal alignment associated with crustal deformation (e.g. Barruol & Kern 1996). During the lateral extrusion over a long period of time (at least since the mid-Miocene) the crystalline structure of the deeper basement rocks likely aligned along this axis, resulting in the fast orientation of Rayleigh waves in the direction of relative motion with respect to the underlying medium. This would imply that the extrusion is at least partly accommodated at crustal depths, and that we are observing its effect in the seismic recordings. We show a schematic view (Fig. 6d) to illustrate how the lateral extrusion may induce fast orientations in the lower crust, whereas the shallow crust is more rigid and largely unaffected by this effect. This may explain why the anisotropy in the deeper crust is generally stronger to the SE of the southern Vienna basin fault. Bianchi & Bokelmann (2014) argue that crystals in the lower crust are instead aligned by the anticlockwise-rotating absolute motion of the Adriatic microplate, suggested by a few anisotropic receiver function measurements that are potentially poorly constrained. Our results do not support this interpretation. Qorbani *et al.* (2016) present results from SKS-splitting in the region, sensitive to anisotropy in the upper mantle. Zhu & Tromp (2013) report fast orientations in the upper mantle from anisotropic adjoint tomography. Both of these studies find fast orientations in the mantle that are roughly perpendicular to our results in the crust. This suggests a decoupling between crust and mantle anisotropy.

5 CONCLUSIONS

We have demonstrated that fast orientations of ambient-noise-derived Rayleigh waves can provide important information at depths, where either stress field or deformation-related crystal alignment strongly affect seismic anisotropy. A prerequisite is to properly correct the group velocities to avoid contamination of the isotropic structure. We indeed find that interpretation of measured Rayleigh wave group velocities in terms of anisotropic structure can be heavily biased by isotropic structure, i.e. the heterogeneous distribution of velocities. However, velocity residuals after isotropic inversion appear to contain mostly anisotropic effects and allow to study the anisotropic structure. This approach can therefore be applied to many already existing data from isotropic velocity models.

Seismic anisotropy in the Vienna Basin area in the topmost kilometers of the crust is apparently controlled by the regional stress field, via crack-induced anisotropy. Fast orientations can be interpreted as orientations of σ_H. This is corroborated by the active faults in the area whose orientation agrees closely with what is expected from the stress-field orientation. At deeper levels in the crust, anisotropy is rather controlled by crystal alignment by deformation due to faults and the lateral extrusion in the area. Orientations agree closely with what is expected from deformation.

ACKNOWLEDGEMENTS

Part of this work was performed using funding from the Austrian Science Fund (FWF): Projects 26391 and 30707. Data were acquired using the ORFEUS web services. The software used in this study was kindly provided by Beyreuther *et al.* (2010) and Herrmann (2013). The data used in this study were provided by operators of the national seismic networks (Austrian Seismic Network 1987; Hungarian National Seismological Network 1992; Czech Regional Seismic Network 1973; National Network of Seismic Stations of Slovakia 2004) and the members of the AlpArray Working Group (AlpArray Seismic Network 2015). We thank the two anonymous reviewers and editor Martin Schimmel for their useful comments and suggestions that helped improve the manuscript. We thank the Alparray Seismic Network Team: G. Hetényi, R. Abreu, I. Allegretti, M.-T. Apoloner, C. Aubert, S. Besançon, M. Bès De Berc, G. Bokelmann, D. Brunel, M. Capello, M. Čarman, A. Cavaliere, J. Chèze, C. Chiarabba, J. Clinton, G. Cougoulat, W. C. Crawford, L. Cristiano, T. Czifra, E. D'alema, S. Danesi, R. Daniel, A. Dannowski, I. Dasović, A. Deschamps, J.-X. Dessa, C. Doubre, S. Egdorf, ETHZ-Sed Electronics Lab, T. Fiket, K. Fischer, W. Friederich, F. Fuchs, S. Funke, D. Giardini, A. Govoni, Z. Gráczer, G. Gröschl, S. Heimers, B. Heit, D. Herak, M. Herak, J. Huber, D. Jarić, P. Jedlička, Y. Jia, H. Jund, E. Kissling, S. Klingen, B. Klotz, P. Kolínský, H. Kopp, M. Korn, J. Kotek, L. Kühne, K. Kuk, D. Lange, J. Loos, S. Lovati, D. Malengros, L. Margheriti, C. Maron, X. Martin, M. Massa, F. Mazzarini, T. Meier, L. Métral, I. Molinari, M. Moretti, H. Munzarová, A. Nardi, J. Pahor, A. Paul, C. Péquegnat, D. Petersen, D. Pesaresi, D. Piccinini, C. Piromallo, T. Plenefisch, J. Plomerová, S. Pondrelli, S. Prevolnik, R. Racine, M. Régnier, M. Reiss, J. Ritter, G. Rümpker, S. Salimbeni, M. Santulin, W. Scherer, S. Schippkus, D. Schulte-Kortnack, v. Šipka, S. Solarino, D. Spallarossa, K. Spieker, J. Stipčević, A. Strollo, B. Süle, G. Szanyi, E. Szücs, C. Thomas, M. Thorwart, F. Tilmann, S. Ueding, M. Vallocchia, L. Vecsey, R. Voigt, J. Wassermann, Z. Wéber, C. Weidle, v. Wesztergom, G. Weyland, S. Wiemer, F. Wolf, D. Wolyniec, T. Zieke and M. Živčić.

REFERENCES

AlpArray Seismic Network, 2015. Temporary component, AlpArray Working Group. Other/Seismic Network. Datacite Link: http://data.datacite.org/10.12686/alparray/z3_2015, doi:10.12686/alparray/z3_2015.

Austrian Seismic Network, 1987. ZAMG, Central Institute for Meterology and Geodynamics, International Federation of Digital Seismograph Networks, doi:10.7914/SN/OE.

Bada, G., Cloetingh, S., Gerner, P. & Horvath, F., 1998. Sources of recent tectonic stress in the Pannonian region: inferences from finite element modelling, *Geophys. J. Int.,* **134,** 87–101.

Bada, G., Horváth, F., Dövényi, P., Szafián, P., Windhoffer, G. & Cloetingh, S., 2007. Present-day stress field and tectonic inversion in the Pannonian basin, *Global Planet. Change,* **58**(1–4), 165–180.

Barruol, G. & Kern, H., 1996. Seismic anisotropy and shear-wave splitting in lower-crustal and upper-mantle rocks from the Ivrea Zone; experimental and calculated data. In Dynamics of the Subcontinental Mantle, from Seismic Anisotropy to Mountain Building (eds. Mainprice, D. and Vauchez, A.), *Phys. Earth planet. Inter.,* **95**(3–4), 175–194.

Beyreuther, M., Barsch, R., Krischer, L., Megies, T., Behr, Y. & Wassermann, J., 2010. Obspy: A python toolbox for seismology, *Seismol. Res. Lett.,* **81**(3), 530.

Bianchi, I. & Bokelmann, G., 2014. Seismic signature of the Alpine indentation, evidence from the Eastern Alps, *J. Geodyn.,* **82,** 69–77, Elsevier Ltd. doi:10.1016/j.jog.2014.07.005.

Boness, N.L. & Zoback, M.D., 2006. Mapping stress and structurally controlled crustal shear velocity anisotropy in California, *Geology,* **34,** 825–828.

Brückl, E., Weber, R., Apoloner, M.-T., Brückl, J., Loderer, W., Maras, J. *et al.*, 2014. ALPAACT - Seismological and Geodetic Monitoring of Alpine-PAnnonian Active Tectonics Final Report 2008–2013. in *Geophysics of the Earth's Crust,* pp. 1–67, Österreichische Akadamie der Wissenschaften.

Czech Regional Seismic Network, 1973. Institute of Geophysics, Academy of Sciences of the Czech Republic, International Federation of Digital Seismograph Networks, doi:10.7914/SN/CZ.

Decker, K. & Burmester, G., 2008. Stress orientations and active fault kinematics of the Vienna Basin Fault System, Aus-rdtria. 3 World Stress Map Conference, 15–17 October 2008, Potsdam, 110.

Decker, K., Peresson, H. & Hinsch, R., 2005. Active tectonics and Quaternary basin formation along the Vienna Basin Transform fault, *Quat. Sci. Rev.,* **24,** 305–320.

Dvorak, V., Dvorakova, L., Ibrmajer, I., Mayerova, M., Mitrenga, P., Naklaalova, Z., Novotny, M. *et al.*, 1990. Vysledky hlubinného vyzkumu kry v Západních Karpatech a na JV svazích Českého masívu, *MS Geofyzika a.s*.

Dziewonski, A., Bloch, S. & Landisman, M., 1969. A technique for the analysis of transient seismic signals, *Bull. seism. Soc. Am.,* **59,** 427–444.

Froment, B., Campillo, M., Roux, P., Gouédard, P., Verdel, A. & Weaver, R.L., 2010. Estimation of the effect of nonisotropically distributed energy on the apparent arrival time in correlations, *Geophysics,* **75,** SA85–SA93.

Fry, B., Deschamps, F., Kissling, E., Stehly, L. & Giardini, D., 2010. Layered azimuthal anisotropy of Rayleigh wave phase velocities in the European Alpine lithosphere inferred from ambient noise, *Earth planet. Sci. Lett.,* **297**(1), 95–102.

Gerner, P., Bada, G., Dövényi, P., Müller, B., Oncescu, M.C., Cloetingh, S. & Horváth, F., 1999. Recent tectonic stress and crustal deformation in and around the Pannonian Basin: data and models, *Geol. Soc., Lond., Spec. Publ.,* **156,** 269–294.

Gribovszki, K. *et al.*, 2017, Estimating the upper limit of prehistoric peak ground acceleration using an in-situ, intact and vulnerable stalagmite from Plavecká priepast cave (Detrekői-zsomboly), Little Carpathians, Slovakia - first results, *J. Seismol.,* **21**(5), 1111–1130.

Gutdeutsch, R. & Aric, K., 1988. Seismicity and neotectonics of the East Alpine-Carpathian and Pannonian Area, in *The Pannonian Basin: A Study in Basin Evolution/Book and Maps (Aapg Memoir),* pp. 183–194, ed. Royden, L.H.

Gutdeutsch, R., Hammerl, C., Mayer, I. & Vocelka, K., 1987. *Erdbeben als historisches Ereignis: Die Rekonstruktion des Bebens von 1590 in Niederösterreich*.

Hammerl, C. & Lenhardt, W., 2013. Erdbeben in Niederösterreich - von 1000 bis 2009 n. Chr.

Hasselmann, K., 1963. A Statistical Analysis of the Generation of Microseisms, *Rev. Geophys.,* **1,** 177–210.

Heidbach, O. *et al.*, 2018. The World Stress Map database release 2016: Crustal stress pattern across scales, *Tectonophysics,* **744,** 484–498, Elsevier. doi:10.1016/j.tecto.2018.07.007.

Herrmann, R.B., 2013. Computer Programs in Seismology: An Evolving Tool for Instruction and Research, *Seismol. Res. Lett.,* **84**(6), 1081–1088.

Hintersberger, E., Decker, K., Lomax, J. & Lüthgens, C., 2018. Implications from palaeoseismological investigations at the Markgrafneusiedl Fault (Vienna Basin, Austria) for seismic hazard assessment, *Nat. Hazards Earth Syst. Sci.,* **18,** 531–553.

Hungarian National Seismological Network, 1992. Kövesligethy Radó Seismological Observatory, Deutsches GeoForschugnsZentrum GFZ, doi:10:14470/uh028726.

Hölzel, M., Decker, K., Zámolyi, A., Strauss, P. & Wagreich, M., 2010. Lower Miocene structural evolution of the central Vienna Basin (Austria), *Mar. Pet. Geol.,* **27,** 666–681 .

Juretzek, C. & Hadziioannou, C., 2016. Where do ocean microseisms come from? A study of Love-to-Rayleigh wave ratios, *J. geophys. Res.,* **121,** 6741–6756.

Kern, H., 1990. Laboratory seismic measurements: an aid in the interpretation of seismic field data, *Terra Nova,* **2,** 617–628.

Kern, H. & Wenk, H.R., 1990. Fabric-related velocity anisotropy and shear wave splitting in rocks from the Santa Rosa Mylonite Zone, California, *J. geophys. Res.,* **95,** 11 213–11 223.

Lee, E.Y. & Wagreich, M., 2017. Polyphase tectonic subsidence evolution of the Vienna Basin inferred from quantitative subsidence analysis of the northern and central parts, *Int J Earth Sci (Geol Rundsch),* **106,** 687–705.

Longuet-Higgings, M.S., 1950. A theory of the origin of microseisms, *Phil. Trans. R. Soc. Lond., A,* **243,** 1–35.

Marsch, F., Wessely, G. & Sackmaier, W., 1990. Borehole-breakouts as geological indications of crustal tension in the Vienna Basin, in *Mechanics of Joined and Faulted Rock,* pp. 113–120, Rossmanith, P.ed., Balkema.

Mordret, A., Shapiro, N.M., Singh, S., Roux, P., Montagner, J.-P. & Barkved, O.I., 2013. Azimuthal anisotropy at Valhall: the Helmholtz equation approach, *Geophys. Res. Lett.,* **40,** 2636–2641.

Nakata, N., Gualtieri, L. & Fichtner, A.eds., 2019. *Seismic Ambient Noise,* Cambridge Univ. Press.

National Network of Seismic Stations of Slovakia, 2004. ESI SAS, Deutsches GeoForschungsZentrum GFZ, doi:10.7914/SN/SL.

Nur, A., 1971. Effects of stress on velocity anisotropy in rocks with cracks, *J. geophys. Res.,* **76,** 2022–2034

Nur, A. & Simmons, G., 1969. Stress-induced velocity anisotropy in rock: an experimental study, *J. geophys. Res.,* **74,** 6667.

Peresson, H. & Decker, K., 1997. The Tertiary dynamics of the northern Eastern Alps (Austria): changing palaeostresses in a collisional plate boundary, *Tectonophysics,* **272,** 125–157.

Qorbani, E., Bokelmann, G., Kovács, I., Horváth, F. & Falus, G., 2016. Deformation in the asthenospheric mantle beneath the Carpathian-Pannonian Region, *J. geophys. Res.,* **121,** 6644–6657.

Ratschbacher, L., Merle, O., Davy, P. & Cobbold, P., 1991. Lateral extrusion in the eastern Alps, Part 1: boundary conditions and experiments scaled for gravity, *Tectonics,* **10,** 245–256

Reinecker, J. & Lenhardt, W.A., 1999. Present-day stress field and deformation in eastern Austria, *Int. J. Earth Sci. (Geol Rundsch),* **88,** 532–550.

Reinecker, J., Tingay, M., Müller, B. & Heidbach, O., 2010. Present-day stress orientation in the Molasse Basin, *Tectonophysics,* **482**(1–4), 129–138.

Robl, J. & Stüwe, K., 2005. Continental collision with finite indenter strength: 2. European Eastern Alps, *Tectonics,* **24,** TC4014, doi:10.1029/2004TC001741.

Schippkus, S., Hausmann, H., Duputel, Z. & Bokelmann, G. the AlpArray Working Group. The Alland earthquake sequence in Eastern Austria: shedding light on tectonic stress geometry in a key area of seismic hazard, *Aust. J. Earth Sci.,* in press.

Schippkus, S., Zigone, D. & Bokelmann, G. the AlpArray Working Group, 2018. Ambient-noise tomography of the wider Vienna Basin region, *Geophys. J. Int.,* **215,** 102–117.

Schmid, S.M., Fgenschuh, B., Kissling, E. & Schuster, R., 2004. Tectonic map and overall architecture of the Alpine orogen, *Eclogae geol. Helv.,* **97,** 93–117.

Smith, M.L. & Dahlen, F.A., 1973. The azimuthal dependence of Love and Rayleigh wave propagation in a slightly anisotropic medium, *J. geophys. Res.,* **78,** 3321–3333.

Taylor, G., Rost, S., Houseman, G.A. & Hillers, G., 2019. Near-surface structure of the North Anatolian Fault zone from Rayleigh and Love wave tomography using ambient seismic noise, *Solid Earth,* **10,** 363–378.

Tsai, V.C., 2009. On establishing the accuracy of noise tomography travel-time measurements in a realistic medium, *Geophys. J. Int.,* **178,** 1555–1564.

Wölfler, A., Kurz, W., Fritz, H. & Stüwe, K., 2011. Lateral extrusion in the Eastern Alps revisited: Refining the model by thermochronological, sedimentary, and seismic data, *Tectonics,* **30**. doi:10.1029/2010TC002782.

Zhu, H. & Tromp, J., 2013. Mapping tectonic deformation in the crust and upper mantle beneath Europe and the North Atlantic Ocean, *Science,* **341,** 871–875.

Zigone, D., Ben-Zion, Y., Campillo, M. & Roux, P., 2015. Seismic tomography of the Southern California Plate boundary region from noise-based Rayleigh and Love waves, *Pure appl. Geophys.,* **172,** 1007–1032.

Zinke, J.C. & Zoback, M.D., 2000. Structure-related and stress-induced shear-wave velocity anisotropy: observations from microearthquakes near the Calaveras Fault in Central California, *Bull. seism. Soc. Am.,* **90,** 1305–1312.

SUPPORTING INFORMATION

Supplementary data are available at *GJI* online.

Figure S1. Measurement of the 2θ- and 4θ-anisotropy terms on all available group velocities for 5 s (a–c) and 15 s (d–f) on measured group velocities (a, d), modelled group velocities (b, e), and group velocity residuals (c, f). Group velocities are binned in 5° azimuth bins and the medians in each bin (black dots) are weighted by standard deviation (error bars). The blue line is the best fitting curve, using the parametrization described in the main text. Strong directional dependence on measured group velocities (left-hand column) is fairly well-explained by modelled group velocities (centre column) from the isotropic velocity model of (Schippkus *et al*. 2018). Residuals show weaker anisotropy on the order of 1 per cent.

Figure S2. Directional dependence (4θ-terms) of group velocities, similar to Fig. 3 (main text). Azimuth limited to 0–90°, because of $\pi/2$-symmetry of the 4θ-term. Low amplitudes ($B \leq 2\%$) for all periods on measured (a), modelled (b) and residual group velocities (c). Fast orientations for measured and modelled group velocities match fairly well. Fast orientations measured on residual group velocities show very low amplitudes with high errors, suggesting that there is no significant contribution of the 4θ-terms.

Figure S3. Numerical simulations of 2θ-parameter-retrieval for 10 000 random sets of interstation group-velocity residuals per period (grey violin plots) and how they compare to the measured parameters (black dots). Each violin plot represents the normalized distribution of the results for all sets for a given period. Available interstation azimuths for each period after applying quality criteria (see Fig. S1) were used for the simulations. On random data, our procedure introduces a slight bias in the retrieved fast orientations for some periods around 0° and 90° (top) due to available interstation paths (see Fig. 2), the azimuth-binning, and very low amplitudes. The consistent fast orientations with period we observe and their significantly higher amplitudes than random group-velocity residuals would yield, however, confirm that the group-velocity residuals do still contain information about the structure of the Earth. While the measured azimuthal anisotropy is weak (A < 2 per cent), the measurements are exceedingly unlikely to be explained by chance, especially considering the consistency of fast orientations and amplitudes over the available period range.

Figure S4. Regionalized azimuthal anisotropy of Rayleigh waves for the available period range (5–20s). The shown periods have their maximum sensitivity to shear velocity at depths of ∼2 km (5 s, a), ∼7 km (10 s, b), ∼11 km (15 s, c), ∼15 km (20s, d), and are sensitive to a broad range of depths (see Fig. 7, main text). Rotation of fast orientations towards east with increasing period. This represents a gradual shift from sensitivity to the shallow stress field at shorter periods (5 s) to sensitivity to mid-crustal deformation at longer periods (20 s), which results in different fast orientations.

Please note: Oxford University Press is not responsible for the content or functionality of any supporting materials supplied by the authors. Any queries (other than missing material) should be directed to the corresponding author for the paper.